ORIGINAL PAPER

Dynamic Mode II Fracture Toughness of Rocks Subjected to Various In Situ Stress Conditions

Wei Yao[1,2] · Jiaxuan Wang[1] · Bangbiao Wu[1] · Ying Xu[1] · Kaiwen Xia[1,3]

Abstract

The shear failure of deep rocks under both a dynamic disturbance and an in situ stress (e.g., preload and confining pressure) is common in deep underground engineering. Thus, it is important to quantify the dynamic mode II fracture toughness K_{IIC} of deep rock considering the in situ stress state. Recently, the punch-through shear (PTS) method and the short core in compression (SCC) method have been successfully adopted to measure the dynamic K_{IIC} of rocks. However, the applicability of these two methods to determine the dynamic fracture toughness K_{IIC} of rocks under preload has not been verified. In this study, the PTS and SCC methods were applied to experimentally measure the dynamic K_{IIC} of rocks subjected to different preload levels. Further, the dynamic K_{IIC} of rocks under various confining pressures was numerically obtained using the SCC method and finite element analysis, because it is difficult to exert the confining pressure on the SCC specimen. The results indicate that the dynamic K_{IIC} of rocks increases with the confining pressure and the loading rate but decreases with the preload, and the total K_{IIC} of rocks derived from the PTS/SCC specimens are almost consistent under the same loading rate regardless of the magnitude of the preload exerted on the PTS/SCC specimens. Another important observation is that the dynamic K_{IIC} of rocks under confining pressures derived from the PTS method is remarkably different from that obtained from the SCC method. Theoretical analysis was conducted to quantitatively rationalize this discrepancy using the difference of the normal stress state and the stress intensity factor in these two methods. An empirical formula was proposed to predict the effect of the loading rate, the confining pressure and the specimen geometry on the dynamic K_{IIC} and to establish the relationship between the dynamic K_{IIC} of rocks measured from the PTS specimen and the dynamic K_{IIC} from the SCC specimen.

Highlights

- Dynamic mode II fracture toughness of rocks under various confining pressures was numerically obtained using the short core in compression method.
- Dynamic mode II fracture toughness of rocks increases with the confining pressure and the loading rate but decreases with the preload.
- Total mode II fracture toughness of rocks are almost consistent under the same loading rate regardless of the preload on the rock specimens.
- There exist remarkable discrepancies of the dynamic rock mode II fracture toughness derived from two testing methods under confining pressures.
- A formula is proposed to predict the effect of the loading rate, the confining pressure and the specimen geometry on the mode II fracture toughness.

✉ Ying Xu
  maggie_xu@tju.edu.cn

1 State Key Laboratory of Hydraulic Engineering Simulation and Safety, School of Civil Engineering, Tianjin University, Tianjin 300072, China

2 State Key Laboratory of Explosion Science and Technology, Beijing Institute of Technology, Beijing 100081, China

3 Department of Civil and Mineral Engineering, University of Toronto, Toronto M5S 1A4, Canada

1 Introduction

Rock structures in complex deep underground geological environment may be prone to collapse and other catastrophes due to the failure under high in situ stresses and dynamic loads. Hence, understanding the process and mechanism of rock fracture under in situ stress is essential for the safe design and assessment of deep underground rock engineering (Kim and Larson 2021; Szwedzicki 2003). There are three fracture modes: mode I (opening mode), mode II (sliding mode or in-plane shear mode), and mode III (tearing mode or out-of-plane shear mode) (Anderson 2005). The fracture toughness, which is defined as the critical stress intensity factor (SIF) at the crack-tip, is used to evaluate the resistance of crack propagation. Consequently, several methods have been developed to determine the fracture toughness under both static and dynamic loading conditions (Chen et al. 2004; Li et al. 2020a, b; Wei et al. 2016a). The methods for measuring the mode I fracture toughness (K_{IC}) have been fully developed. For example, the circle bending (CB) specimen and the short rod (SR) specimen have become suggested methods recommended by the International Society of Rock Mechanics and Rock Engineering (ISRM) (Franklin et al. 1988; Mostafavi et al. 2013; Zhang et al. 1999), and other methods (e.g., the cracked chevron notched Brazilian disc (CCNBD) (Fowell 1995), the semi-circular bend (SCB) (Kuruppu et al. 2014; Wei et al. 2016b), the notched semi-circular bending (NSCB) (Kuruppu et al. 2014; Wei et al. 2016a; Zhou et al. 2012) have also been proposed to measure the K_{IC} value of rocks under both dynamic and static loading condition.

In deep rock engineering, the shear or compression-shear mixed failures are the most common disasters due to the crack/defect instable propagation inside rocks under high in situ stress states and dynamic disturbances. Therefore, the static and dynamic mode II fracture properties of rocks are crucial to reveal the failure mechanism of deep rock structures and to effectively assess the stability and safety of deep underground rock engineering (Wei et al. 2017; Xu et al. 2016, 2020). A variety of methods have been proposed to measure the static mode II and mixed I/II fracture toughness of rocks by applying shear loads to pre-cracked specimens (Xu et al. 2020). For instance, antisymmetric four-point bending specimen has been used to obtain the static mode II fracture toughness (K_{IIC}) of rocks in the shear fracture testing (Fakhri et al. 2017; Razavi et al. 2017; Shi and Zhou 1995; Swartz et al. 1988). Arcan specimen with a prefabricated crack is suitable to conduct the fracture testing for multiple fracture modes in a uniform plane stress state and static loading condition (Hasanpour and Choupani 2008). The semi-circular bend (SCB) specimen can be manufactured with an oblique notch or using various types of support to obtain the mixed mode I/II fracture toughness (Chang et al. 2002; Pirmohammad et al. 2021; Xie et al. 2017). Moreover, the cracked straight-through Brazilian disc (CSTBD) was employed to determine the K_{IIC} value of rocks under the quasi-static loading (Azar et al. 2015). However, the crack propagation directions in these specimens mentioned above generally deviate from the direction of the pre-crack during the loading period because of the specimen geometry and the loading mode, implying that the crack growth path is not along the direction of the maximum shear stress and the mode II fracture toughness measured from these methods is doubtable (Rao et al. 2003). Therefore, a shear box test with prefabricated cracks on each side of the specimen was developed to avoid the weakness of previous methods, i.e., fractures propagate along the direction of the maximum shear stress and the pure mode II fracture can be obtained in this method (Rao et al. 2003). In addition, the punch-through shear (PTS) experiment with confining pressure has been developed (Backers 2005; Backers et al. 2002, 2004; Davies et al. 1985) and recommended by the ISRM as a suggested method to quantify the static K_{IIC} of rocks (Backers and Stephansson 2012). Meanhile, the PTS method has been extend to the rectangular specimen under biaxial loading to measure the static K_{IIC} of rocks (Lee 2007). Although the PTS method is a core-based specimen and facilities the confining pressure assembly, the specimen preparation is cumbersome. Hence, a short beam in compression (SBC) method was adopted to quantify the static K_{IIC} of rock-like materials because of the simple specimen preparation and assembly (Watkins and Liu 1985; Whittaker et al. 1992). Recently, Jung and Park (2016) designed a short core in compression (SCC) method by combining the PTS and SBC and changing the cuboid specimen into a cylindrical core specimen. Xu et al. (2020) assessed the validation of the SCC method for obtaining the static K_{IIC} of rocks.

As discussed above, most of methods above were valid to measure the mode II and mixed I/II fracture toughness of rocks under static or quasi-static loading. In practice, the underground rocks are likely to failure due to dynamic disturbances, such as explosions, earthquakes, and mineral mining. Thus, the dynamic mode II fracture properties of rocks have been extensively investigated (Heritage 2019; Lukić and Forquin 2016; Peng et al. 2020; Yao et al. 2017, 2019, 2021). The existing studies show that the K_{IIC} values

of rocks strongly depend on the loading rate and the confinement/hydrostatic pressure (Heritage 2019; Peng et al. 2020; Yao et al. 2017, 2019, 2021). Generally, the dynamic K_{IIC} increases with the increase of the confining pressure. Additionally, several apparatuses have been developed to perform the dynamic fracture experiments for rocks under in situ stress states (such as hydrostatic and preload) based on a split Hopkinson pressure bar (SHPB) system (Frew et al. 2010; Li et al. 2007; Wu et al. 2015; Yao et al. 2019; Zhou et al. 2020, 2014). By using these testing systems, the dynamic K_{IC} of rocks under different confining pressure/hydrostatic pressure were systematically measured (Chen et al. 2016; Yao et al. 2019; Yin et al. 2018). In our previous studies, both the PTS and SCC specimens have been extended to measure the dynamic K_{IIC} of rocks, and the dynamic K_{IIC} and failure mode of rocks under hydrostatic and confinement conditions were discussed by using these two specimens (Yao et al. 2020, 2021). However, there is no investigation to measure the dynamic K_{IIC} of rocks under the preload and to further compare the dynamic K_{IIC} of rocks under complex stress states derived from the PTS specimen with that from the SCC specimen. To fill such a research gap, in this study, the PTS and SCC methods were applied to obtain the dynamic mode II fracture toughness of rocks under preload and confinement conditions. The dynamic mode II fracture tests were performed by using the dynamic-static-combined test apparatus. In addition, due to the limitation of the existing triaxial SPHB apparatus and the geometry of the SCC specimen, the numerical simulation was used to mimic the dynamic mode II fracture test with

high confinement levels using the SCC specimen. Theoretical analysis was conducted to quantitatively rationalize this discrepancy of the dynamic K_{IIC} of rocks under confining pressures derived from the PTS method and the SCC method. An empirical formula was proposed to establish the relationship between the dynamic K_{IIC} of rocks measured from the PTS specimen and the SCC specimen.

2 Methodology

2.1 Specimen Preparation for Dynamic PTS and SCC Tests with Preload

The PTS and SCC specimens were made of Fangshan marble (FM) from Beijing, China. The basic properties of FM are given in Table 1. The geometry of the dynamic PTS specimen in our earlier study was selected in this study (Yao et al. 2020), as shown in Fig. 1. The PTS specimen is a 54 mm × 30 mm cylindrical specimen with two notches (10 mm height and 1.5 mm thickness) at the upper and lower end of the specimen. The inner diameter (ID) of the PTS specimen is 25.4 mm. Under the compressive loading, the shear stress is produced in the truncated cone-shape bridge between two notch-tips. In addition, the SCC specimen with a 38 mm-diameter (Fig. 2) was used in this study (Yao et al. 2021). Two parallel half-through notches were machined from opposite sides and the fronts of these two notches are parallel. The distance between the notch and its nearest core end is the same. The shear failure occurs in the rectangular

Table 1 The basic properties of FM (Zhang QB 2013a, b)

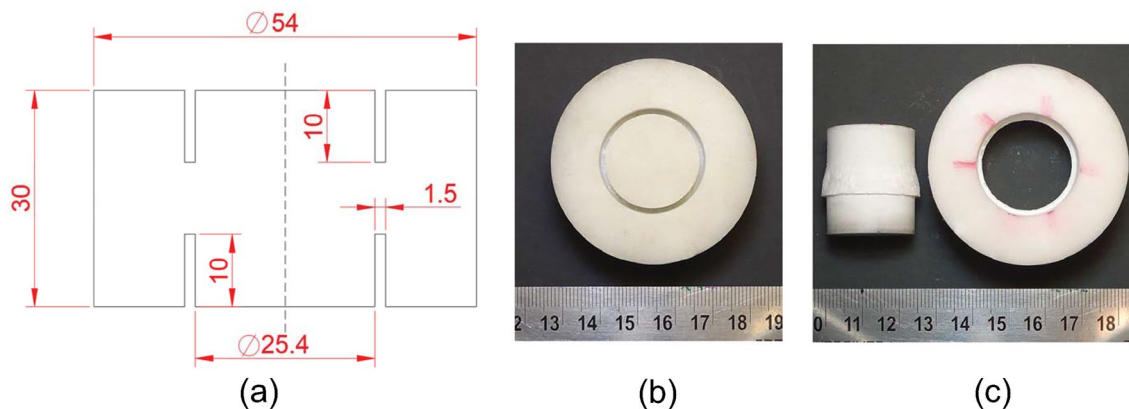| Density ρ	Young's modulus E	Poisson's ratio ν	P-wave velocity C_p	Compressive strength σ_c	Tensile strength σ_t	Mode I fracture toughness K_{IC}
2.85 g/cm³	85 GPa	0.3	5900 m/s	155 MPa	9.5 MPa	1.5 MPa·m$^{1/2}$

Fig. 1 **a** The dimension of the dynamic PTS specimen; **b** A typical original PTS specimen; **c** A typical tested PTS specimen
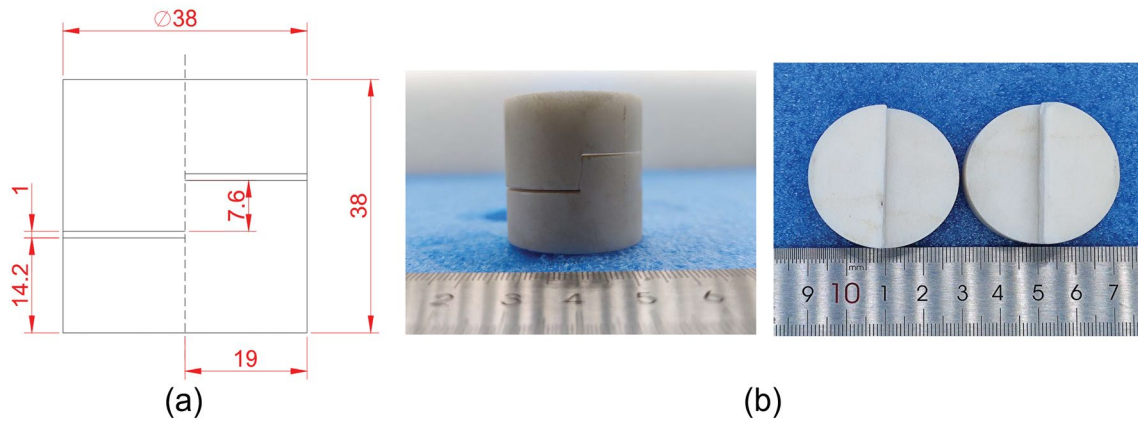
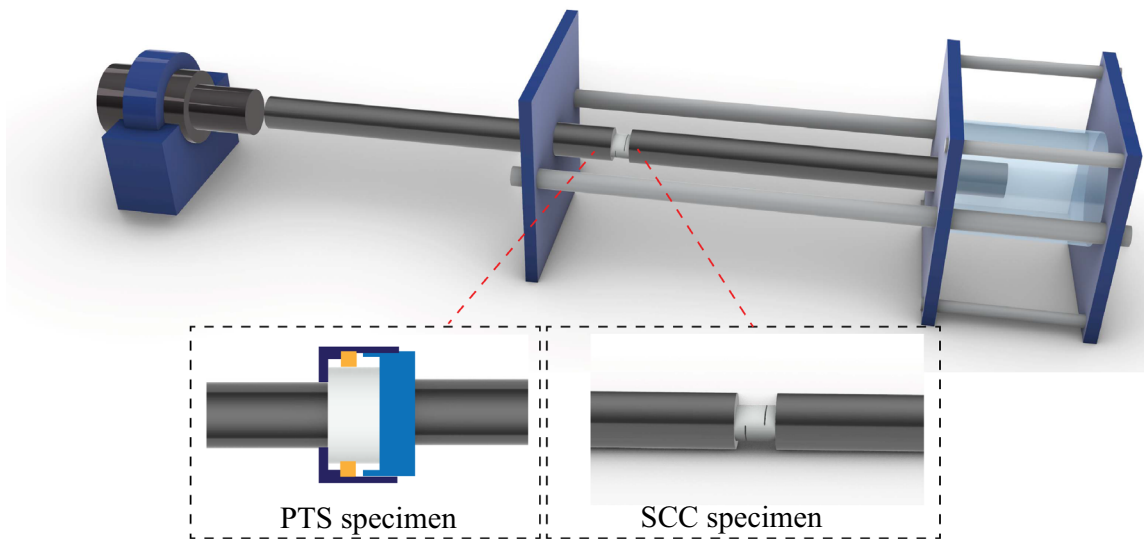Fig. 2 **a** The dimension of the dynamic SCC specimen and **b** a typical tested SCC specimen

bridge between two notch-tips when the two ends of the SCC specimen are under the compressive loading. The notch width of the PTS and SCC specimens is 1 mm and 1.5 mm, respectively. In the specimen preparation, the FM bock was drilled into cores with desired diameters, and the cores were then cut into cylinders with specific thicknesses. Thereafter, the corresponding notches were machined on the PTS and SCC specimens, respectively. Moreover, the end of the cylindrical specimens is perpendicular to its longitudinal axis within 0.5° and is flat to 0.1 mm, and the surface and the groove of the specimens are smooth.

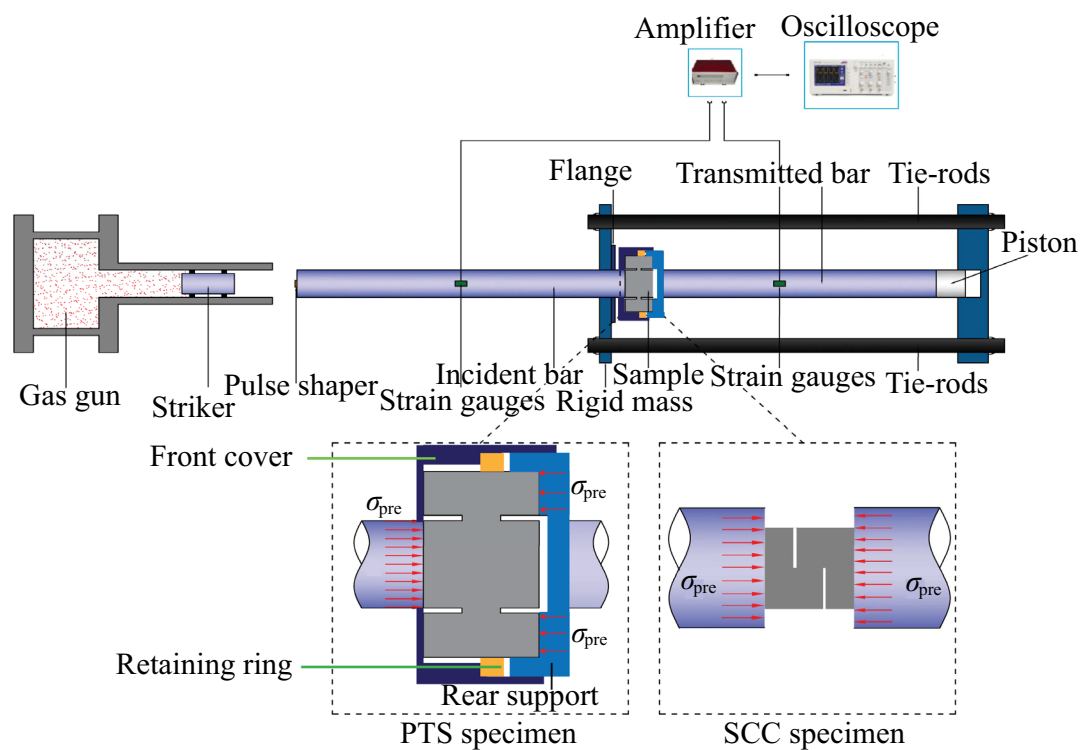## 2.2 Experimental System for Dynamic PTS and SCC Tests with Preload

A dynamic-static-combined testing apparatus was employed to conduct the dynamic PTS and SCC experiment with a static preload (Yao et al. 2020). As shown in Fig. 3, this dynamic-static-combined testing apparatus comprises a static preload system and a traditional SHPB system (including a striker, an incident bar, and a transmission bar) with a data acquisition system. The static preload system mainly consists of a hydro-cylinder and a rigid mass attached at the incident bar via a flange (Wu et al. 2015). High hydraulic pressure in the cylinder provides an axial preload to the piston. This axial preload is delivered to the transmitted bar and the specimen, because two tie-rods fix the leftward movement of the chamber and the incident bar. The preload level is determined by the hydraulic pressure, which is precisely operated by a hydraulic control system. The specimen is generally located between the incident and transmitted bars. In this study, two SHPB systems with different bar-diameters were used to suit the different dimensions of the PTS and he SCC specimens, respectively. All bars are made of Maraging steel. For the dynamic PTS test, the bar with the diameter of 25.4 mm was utilized as the load stamp to fit the ID of

the PTS specimen, and a front cover and a rear supporter made of stainless steel were employed to accommodate shear deformation in the specimen. The design of the front cover and the rear supporter can be found in our early work (Yao et al. 2017). A groove was made in the rear supporter to assemble to the transmitted bar (as shown in Fig. 3b). Also, a retaining ring was used to ensure that the axis of the incident bar is aligned with the axis of the PTS specimen. The preload was exerted on the PTS specimen through the rear supporter to achieve the shear stress in the shear bridge. For the SCC specimen, the bar with the diameter of 50 mm was employed to guarantee the end of the SCC specimen can be covered by the end of bars (as shown in Fig. 3b). In such case, the compressive preload on the ends of the SCC specimen can generate the shear stress in the shear bridge. The data acquisition system in this study satisfies the requirements in the ISRM suggested method for determining the dynamic properties of rocks (Zhou et al. 2012).

During the dynamic experiments, the preload with a designed value was first applied to the ends of the specimen, followed by the impact of the striker on the free end of the incident bar. As a result, an incident stress wave (ε_i) was generated in the incident bar, and the incident wave propagated along the incident bar without being affected by the flange, because the impact motion of the bars is rightward and the mass of the flange is tiny (~ 10 g in mass) (Wu et al. 2015). When the incident wave arrives the flange, the motion rightward of the flange and the incident bar was not restrained and thus the incident bar and the tiny flange can freely move rightward. Consequently, the incident wave can propagate smoothly along the incident bar. Thereafter, the transmitted waves (ε_t) and the reflected waves (ε_r) were produced when the incident stress wave reaches the bar-specimen interfaces. The signals of the stress waves ε_i, ε_t and ε_r were measured through strain gauges on the surface of two bars (Fig. 3b).

Fig. 3 **a** Schematic and **b** details of a dynamic-static-combined testing system with a preload system

In addition, the force balance at two ends of the specimen is the prerequisite of the valid dynamic rock test and thus the pulse shaper (Fig. 3b) was utilized in this study as the recommendation by the ISRM. Figure 4 illustrates the dynamic force history in a typical SCC and PTS tests. It is obvious that the dynamic force equilibrium is reached, i.e., $P_1(t) \approx P_2(t)$, where P_1 and P_2 is the dynamic forces on the ends of the specimen, and can calculated using the stress waves:
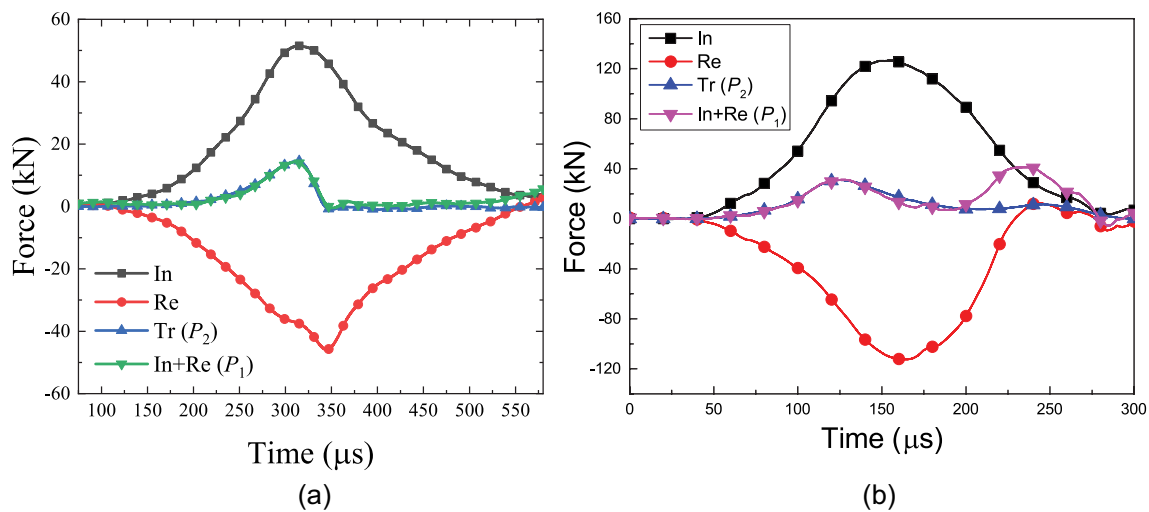
Fig. 4 Dynamic force equilibrium in a typical, **a** dynamic SCC test and **b** dynamic PTS test

$$P_1 = A_b E_b \big(\varepsilon_i(t) + \varepsilon_r(t) \big), \quad P_2 = A_b E_b \varepsilon_t(t), \quad (1)$$

where A_b and E_b are the cross-sectional area and Young's modulus of bars, respectively. The force balance was achieved for all dynamic PTS and SCC tests in this study.

In this study, different preload values were determined based on the static critical load of the specimen, which is defined as a critical external load on the PTS/SCC specimen when the failure occurs under a static load. The static critical load for the PTS specimen differs from that for the SCC specimen due to the different geometries of these two specimens. The critical external load of the PTS specimen (i.e., 34.456 kN) in the previous study was adopted in this study (Xu et al. 2020). A computer-controlled electronic universal testing machine was used to measure the static critical load of the SCC specimen. The load and displacement in this machine were automatically controlled, and the maximum load capacity is 50 kN. The loading speed was a constant displacement rate of 0.05 mm/min. The SCC specimens were under the quasi-static uniaxial compressive loading and the histories of compressive stresses were recorded. The value of the preload for the SCC specimen was determined by averaging the peak compressive stresses measured from three repetitive tests to reduce the error. Typical compressive loading histories for the SCC specimens are shown in Fig. 5, and the average value of the critical external load of the SCC specimen is 5.366 kN and the corresponding compressive stress on the end of the SCC specimen is 4.732 MPa. For each type of specimen, the preload values were chosen as 0%, 20%, 40%, 60% and 80% of the corresponding critical load.
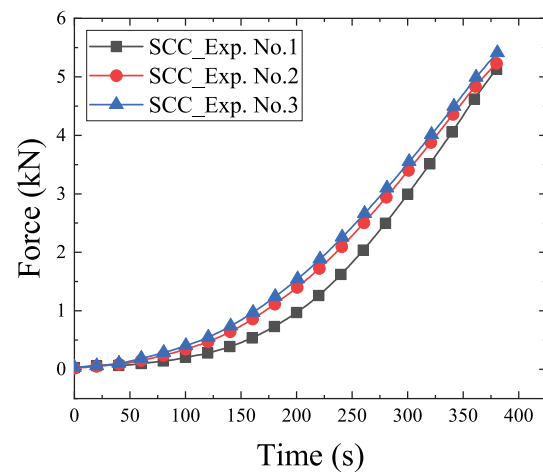

Fig. 5 Typical compressive loading histories for the SCC specimen in the quasi-static tests

2.3 Dynamic SCC Numerical Simulation with Confinement

In the dynamic SCC-SHPB experiment with the confinement, the confinement should be appropriately applied on the side of the SCC specimen and there is no confining pressure in two notches, as shown in Fig. 6. In the existing dynamic testing system with the confinement, the confinement was generally applied on the specimen through the Hoek cell or a confinement cylinder (Yao et al. 2019, 2020). Consequently, it is hard to guarantee that the confinement completely and appropriately exerts on the sides of the SCC specimen under high confining pressures without destroying the confining loading device or applying extra force on the sharp corner of the notches. Thus, it is difficult to conduct
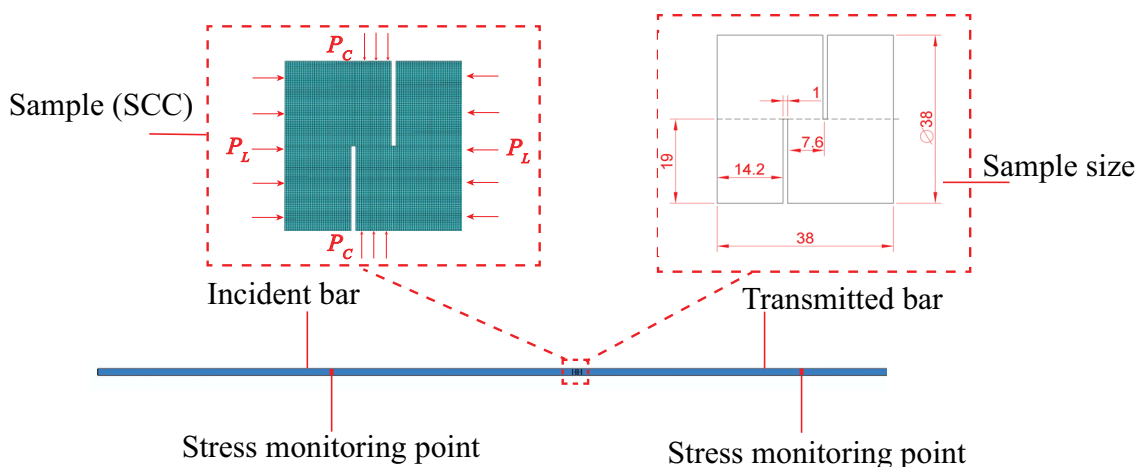
Fig. 6 Numerical dynamic SCC-SHPB model

the dynamic mode II fracture test with high confinement levels through the SCC specimen due to the limitation of the existing triaxial SPHB apparatus and the geometry of the SCC specimen. In this study, to overcome the limitation of the experimental apparatus, the numerical simulation was used to mimic the dynamic mode II fracture test with high confinement levels using the SCC specimen. As shown in Fig. 6, a two-dimensional (2D) finite element model was built via a commercial program ABAQUS. The model consists of the incident bar, the transmitted bar, and the rock SCC specimen. The incident bar, the SCC specimen and the transmitted bar are composed of 8671, 8976 and 8671 elements, respectively. The histories of the dynamic stress waves (i.e., ε_i, ε_t and ε_r) were extracted from the stress monitoring points (Fig. 6) in the incident bar and the transmitted bar. The diameter and the length of the bars are the same as those in the dynamic SCC-SHPB experiments, i.e., the diameter of 50 mm for two bars, the length of 2500 mm and 1500 mm for the incident bar and the transmitted bar, respectively. The elastic properties of the bars in the numerical model include Young's modulus of 200 GPa, Poisson's ratio of 0.2, and the density of 7.85 g/cm^3. Moreover, the dimensions of the numerical SCC specimen model are shown in Fig. 6 (which is the same as those of the SCC specimen in the dynamic SCC-SHPB experiment). Also, the elastic properties (including Young's modulus, Poisson's ratio, and the density) of the numerical SCC specimen are listed in Table 1. Furthermore, based on the force balance principle, the confining pressure on the entire side of the SCC specimen in the simulation can be simplified as the confining pressure on the shear bridge of the SCC specimen (as shown in Fig. 6).

Without the striker in the SCC-SHPB simulation, the incident waves under different loading rates, which were generated based on the incident waves in the dynamic

SCC-SHPB experiments, were imported in the numerical model and directly applied to the free end of the incident bar. A typical incident wave used in the numerical simulation was shown in Fig. 7. The dynamic loading forces on two ends of the SCC specimen were derived from the stress monitoring points on bars and then calculated by using Eq. (1). Figure 7 illustrates the histories of the dynamic loading forces in a typical numerical SCC-SHPB test with the confinement, indicating that the dynamic force equilibrium of the SCC specimen under the confining pressure was achieved in the numerical model. Meanwhile, the failure criterion is important to obtain an accurate result in the numerical simulation. Drucker-Prager (D-P) criterion was developed based on the Mohr–Coulomb (M-C) theory (Deng et al. 2006; Su et al. 2003). Compared with the M-C theory, the D-P criterion on the π plane is a circle and the yield
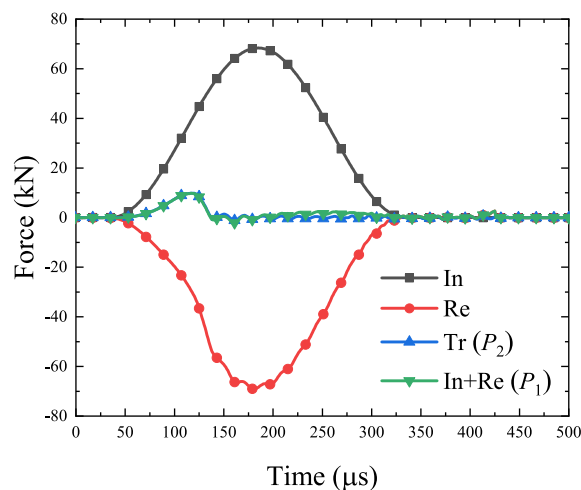

Fig. 7 Dynamic force equilibrium in a typical dynamic numerical SCC test with the confinement

surface in the principal stress space is a smooth cone. Thus, the influences of both the intermediate principal stress and the hydrostatic pressure on the failure process are considered in the D-P criterion, which overcomes the main weakness of the M-C criterion. Moreover, the classical D-P criterion was extended in ABAQUS. i.e., the shape of the yield surface on the meridional surface can be simulated by a linear function, a hyperbolic function or an exponential function model. Also, a modified D-P cap model with a cap yield surface in ABAQUS can provide the shear failure of the material. Additionally, the modified D-P model has a simple expression and high calculation efficiency. Therefore, the modified Drucker-Prager criterion was adopted in the numerical SCC-SHPB model to determine the dynamic K_{IIC} of FM. In this study, the dynamic mode II fracture toughness obtained from the numerical SCC-SHPB model was first compared with the data measured from the dynamic SCC-SHPB experiments without the confinements/the preloads. If the results obtained from the numerical SCC-SHPB model are consistent with those from the dynamic SCC-SHPB experiments without the confinements/the preloads, it means that the numerical SCC-SHPB model is valid to obtain the dynamic mode II fracture toughness of FM under the confinements or the preloads. Thus, the numerical SCC-SHPB model was first calibrated by using the dynamic K_{IIC} of FM without the confinement measured from the dynamic SCC-SHPB experiments, and then the validated numerical SCC-SHPB model was employed to obtain the dynamic K_{IIC} of FM under various loading rates and confining pressures.

3 Determination of Stress Field and SIF of PTS and SCC Specimens

3.1 Comparison of Stress Fields Between PTS and SCC Specimens

A 2D finite element model was constructed by using ABAQUS to investigate the stress fields of the PTS and SCC specimens under the confinement and the preload conditions. The geometries of the PTS and SCC specimens are the same as those of the specimens used in the dynamic experiments (Figs. 1c and 2c). Figure 8 shows the loads and constrains of the PTS and SCC specimens in the finite element analysis (FEA). According to the distribution of the confining pressure P_c, the confining pressure out of the range of the shear zone can be offset due to the symmetry of the PTS and SCC specimen models and thus the confining pressure out of the range of the shear zone do not have a contribution to the initiation and the propagation of the shear fracture in the PTS and SCC specimens. In such a case, the confining pressure exerted on the PTS and SCC specimens within the range of the shear zone is enough to simulate the shear failure of the PTS and SCC specimen under the confinement, as shown in Fig. 8. In this study, only half of the PTS specimen was built in the FEA because of the symmetry of the PTS specimen. These PTS and SCC models consist of 21,500 and 8976 elements, respectively. The Young's modulus and the Poisson's ratio in these EFA models are chosen in Table 1. In addition, the confining pressures P_c on both PTS and SCC specimens were selected as 5 MPa, 10 MPa, 15 MPa, 20 MPa, which is the same as those in the dynamic PTS and SCC experiments. As shown in Fig. 8, the force P_L is used to generate the shear stress in these two types of specimens. Similar to the dynamic PTS and SCC experiments, the effective force (i.e., $P_L = 1.134$ kN) was exerted on both the PTS and SCC specimens in this simulation in order to efficiently compare

Fig. 8 Loading scheme of **a** the SCC specimen and **b** the PTS specimen in the numerical analysis (P_L is preload (Unit: kN) and P_c is confining pressure (Unit: MPa))
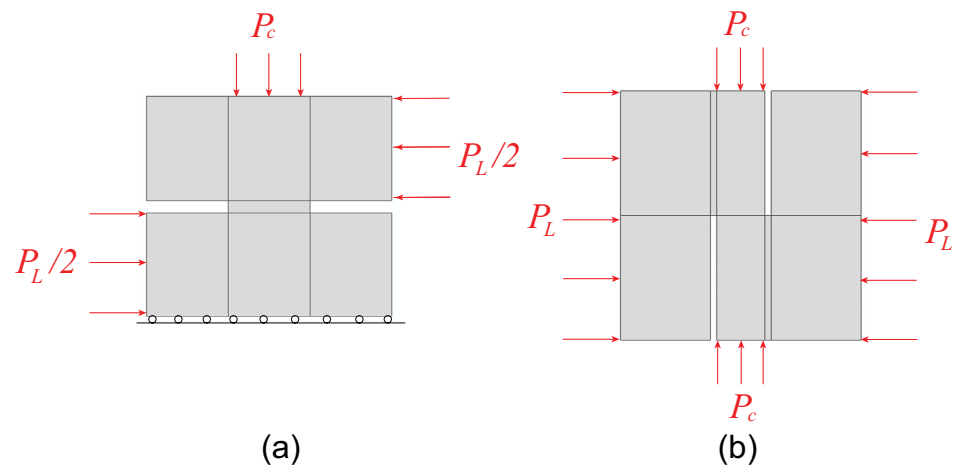
the stress field in these two types of specimens. It is obvious that the loading area on the PTS specimen is different from that on the SCC specimen. Hence, the effective uniformly distributed stress applied on the PTS specimen is different from that on the SCC specimen to guarantee that the effective force on both the PTS and SCC specimen is consistent.

The shear stress fields of the PTS and SCC specimens under different confining pressures are systematically compared in Fig. 9. For the PTS and SCC specimens, the stress concentration can be observed for all confinement levels on at the notch-tips, where the shear cracks are initiated. The maximum shear stresses in the SCC specimen appear at both two notch-tips for all confinement levels, while the maximum shear stresses in the PTS specimen occurs at one notch-tip for all confinement levels. With the increase of the confining pressure, the shear stress increases for both the PTS and SCC specimens. A shear zone between two notch-tips in the PTS and SCC specimens can be identified when the confining pressure is low (e.g., 0 MPa and 5 MPa). The shear stress in the PTS and SCC specimens degenerates into lower values in the middle between these two notch-tips (which are close the values of the stress around the shear bridge) if the confining pressure is high (e.g., 15 MPa and 20 MPa). In addition, it is noteworthy that at the same loading force and confining pressure, the shear stress at the notch-tip in the PTS specimen is much higher than that in the SCC specimen. Consequently, the SIFs generated at the notch-tips are distinct in these two types of specimens under the same loading force and confining pressure. This causes that the critical load of the PTS specimen differs from that of the SCC specimen.

The shear stress fields of the PTS and SCC specimens under different preloads were obtained by using these FEA models without the confinement. As we discussed above, the critical external load of the PTS specimen is different from that of the SCC specimen. Similar to the experiments with preloads, the preloads for the PTS specimen in the simulation were chosen as 20%, 40%, 60%, and 80% of the corresponding critical load of $P_{SCC} = 5.366$ kN, and the preloads of the SCC specimen as 20%, 40%, 60%, and 80% of the corresponding critical load of $P_{PTS} = 34.456$ kN. Figure 10 illustrates the static shear stress fields of PTS (left) and SCC (right) specimens at different preloads. The distributions of shear stress in the PTS specimen at various preloads are identical and these distributions in the SCC specimen at various preloads are also the same. For both the PTS and SCC specimens, the stress concentration can be observed for all preloads on at the notch-tips, where the shear cracks are initiated. The maximum shear stresses in the SCC specimen appear at both two notch-tips for all preloads, whereas the maximum shear stresses in the PTS specimen occurs at one notch-tip for all preloads. Meanwhile, with the increase of the preload, the maximum value of the shear stress increases in both the PTS and SCC specimens. A shear zone

between these two notch-tips in the PTS and SCC specimens can be identified for all preload conditions. It is noteworthy that the shear stresses generated at the notch-tips are distinct in these two types of specimens at the same percentage of the corresponding critical load. This implies that the SIF at the notch-tip of the PTS specimen is different from that of the SCC specimen when the PTS and SCC specimens fail at their respective critical loads.

To clearly understand the difference between the SIF at the notch-tip of the PTS and SCC specimens, the finite element models were constructed for the PTS and SCC specimens with secondary shear cracks. The singular and quadrilateral eight-mode elements CPS8R in ABAQUS were used at the notch-tip to simulate the singularity at the shear notch-tips as shown in Fig. 11. Similarly, only half of the PTS specimen was built due to its symmetry. The PTS and SCC models consists of 17,762 and 4516 elements, respectively. The loads and constrains for these models are schematically shown in Fig. 8. The variations of the SIF K^*_{II} at the notch-tip in terms of the confining pressure and the axial compressive load are given in Fig. 12a and b, respectively. Under the same confining pressure, the K^*_{II} value of the PTS specimen is lower than that of the SCC specimen. With the increase of the confining pressure, the slope of the K^*_{II}—time line for the PTS specimen is higher than that for the SCC specimen (Fig. 12a), indicating that the K^*_{II} of the PTS specimen is more sensitive to the confinement variation than that of the SCC specimen. In addition, the K^*_{II} values of the PTS and SCC specimens increase with the axial compressive load. As shown in Fig. 12b, the slope of K^*_{II}—time line for the PTS specimen is obviously smaller than that for the SCC specimen. This demonstrates that the axial compressive load applied on the PTS specimen is much greater than that on the SCC specimen when the same K^*_{II} value was achieved at the notch-tip of both PTS and SCC specimens.

3.2 Determination of the SIF of PTS and SCC Specimens

According to the ISRM suggested method (Backers and Stephansson 2012), the SIF K^*_{II} at the notch-tip of the PTS and SCC specimens under the preload can be expressed as

$$K_{II}^{tp*} = \alpha(\sigma + \sigma_{\mathrm{pre}}), K_{II}^{dp*} = \alpha\sigma. \tag{2}$$

Meanwhile, the SIF K^*_{II} at the notch-tip of the PTS and SCC specimens under the confining pressure can be written as

$$K_{II}^{dc*} = \alpha\sigma + \beta\sigma_c, \tag{3}$$

where K_{II}^{tp*} is the total SIF of rocks under both the dynamic load and the preload, K_{II}^{dp*} is the SIF of rocks due to the dynamic load, K_{II}^{dc*} is the SIF of rocks under the dynamic

Fig. 9 Static shear stress (Unit: MPa) field of the PTS (left) and SCC (right) specimens under the confining pressure of **a** 0 MPa; **b** 5 MPa; **c** 10 MPa; **d** 15 MPa; **e** 20 MPa (The loading scheme of the PTS and SCC specimen is the same as that in Fig. 8a and b, respectively.)

(a)

(b)

(c)

(d)

(e)
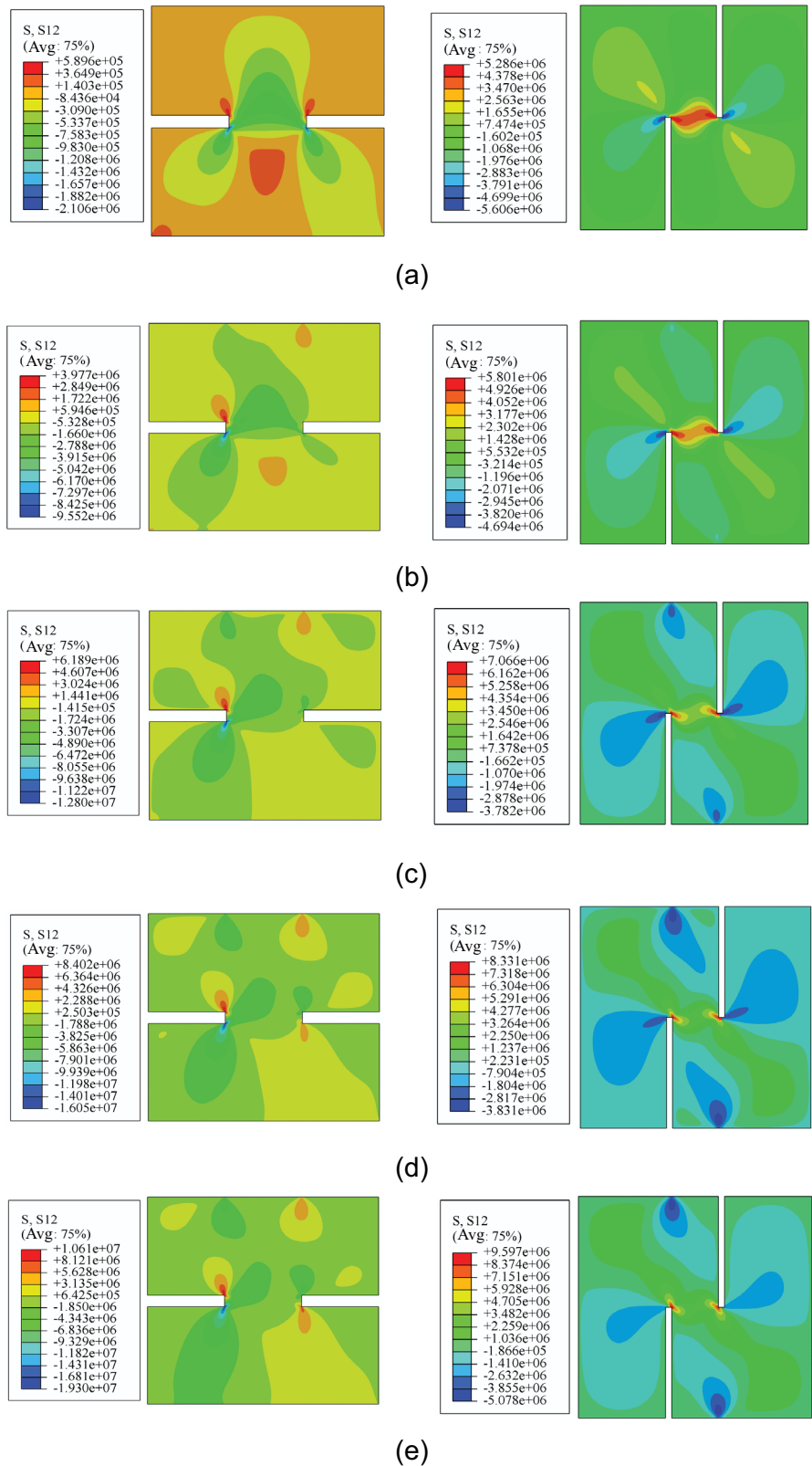
load and the confinement, σ is the dynamic compressive stress on the ends of PTS/SCC specimens (MPa), σ_{pre} is the compressive stress due to the preload on the ends of PTS/

SCC specimens (MPa), σ_c is the confining pressure (MPa) on the PTS/SCC specimens, α and β are geometrical parameters. For the PTS specimen, the values of α and β were

Fig. 10 Static shear stress (Unit: MPa) field of the PTS (left) and SCC (right) specimen at the preload of **a** 20% P_{PTS} for the PTS specimen (left) and 20% P_{SCC} for the SCC specimen (right); **b** 40% P_{PTS} for the PTS specimen (left) and 40% P_{SCC} for the SCC specimen (right); **c** 60% P_{PTS} for the PTS specimen (left) and 60% P_{SCC} for the SCC specimen (right); **d** 80% P_{PTS} for the PTS specimen (left) and 80% P_{SCC} for the SCC specimen (right) (The loading scheme in this figure is shown in Fig. 7.)

(a)

(b)

(c)

(d)
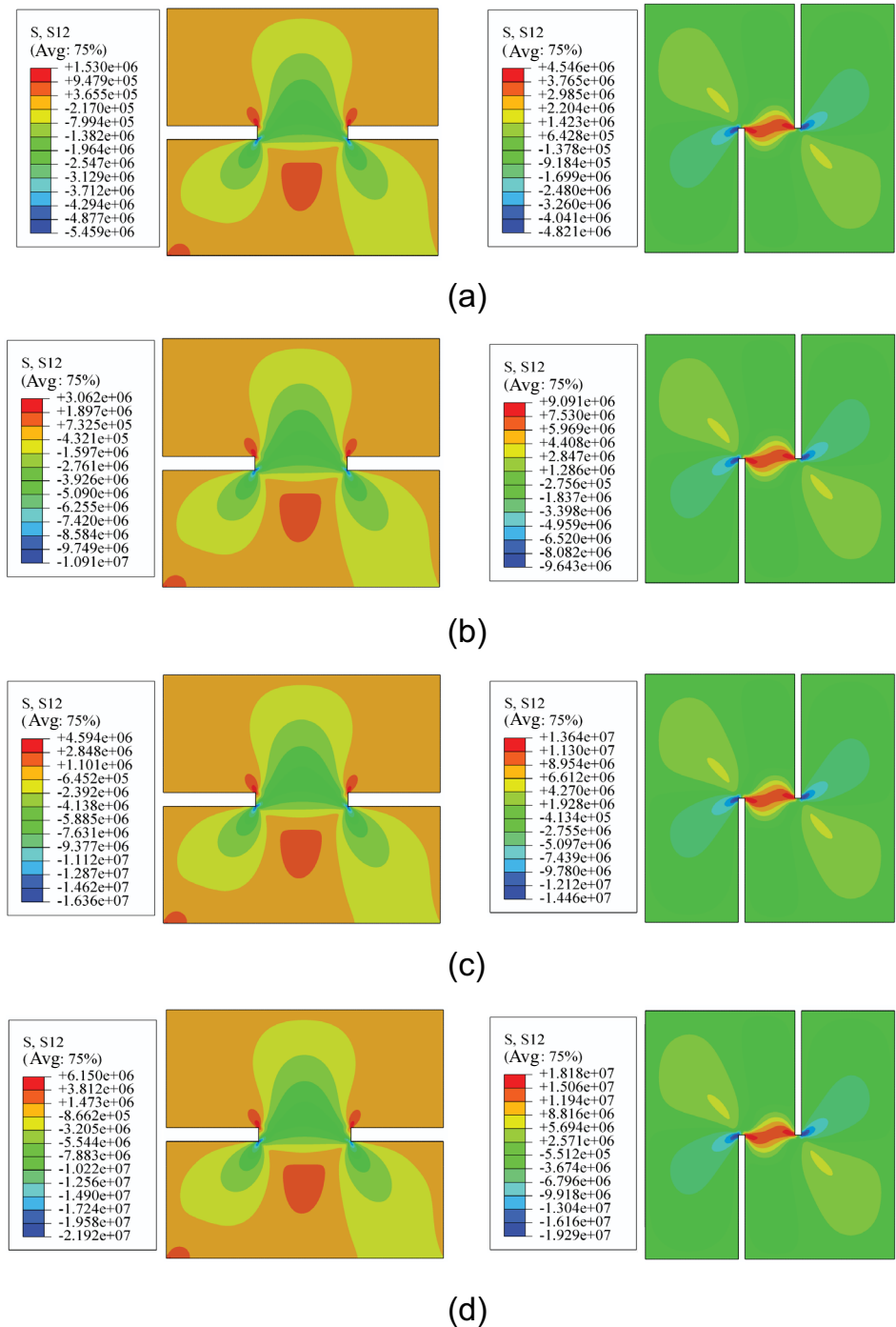
determined by using the displacement extrapolation technique (DET) and a finite element analysis (FEA) with the geometry of the dynamic specimen used in both our previous studies and this study. According to the previous studies (Yao et al. 2020, 2021), the values of α for the PTS and SCC specimens in this study are 0.04192 m$^{1/2}$ and 0.27 m$^{1/2}$, respectively. The value of β for the PTS specimen in this study is -5.6×10^{-3} m$^{1/2}$, while the value of β for the SCC specimen can be obtained by the numerical simulation in a

combination of the *J*-integral method and the displacement extrapolation technique (Xu et al. 2020; Zhou et al. 2012). In this study, the SIF is directly determined by using the numerical simulation and thus it is unnecessary to calculate the value of β for the SCC specimen.

Due to the dynamic force balance in the specimen, the SIF of the PTS and SCC specimens under dynamic loading period can be derived from Eqs. (2) and (3) for the preload and confinement conditions, respectively:
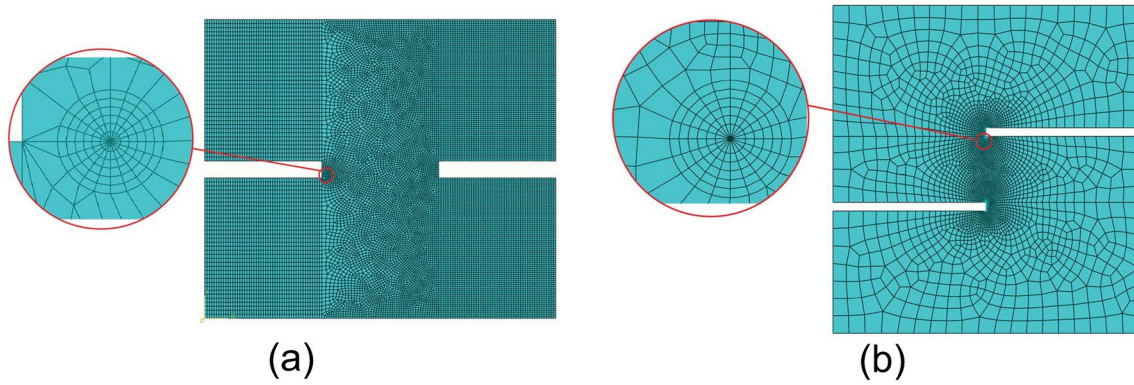
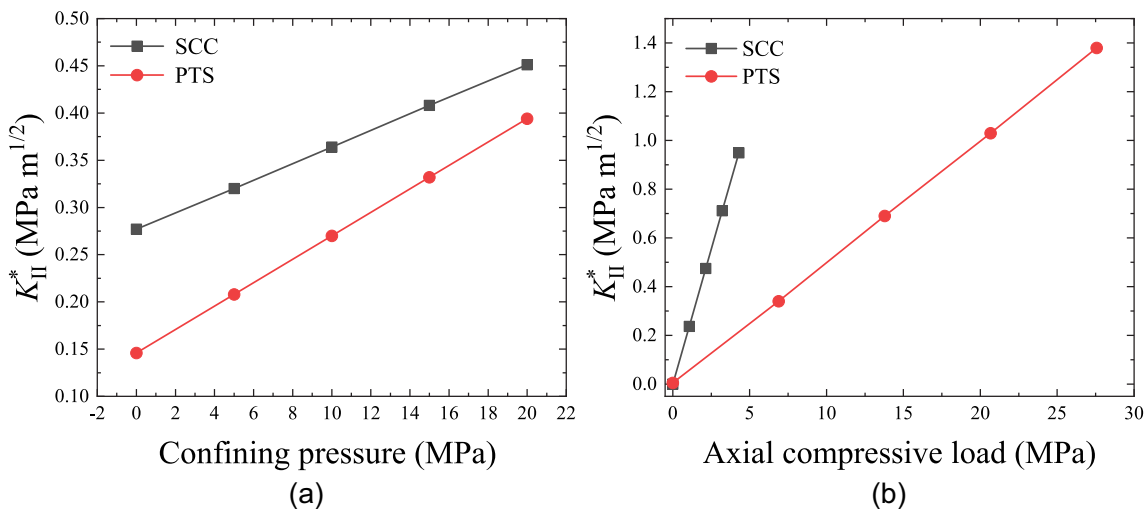**Fig. 11** Meshing scheme of **a** the PTS specimen and **b** the SCC specimen

Fig. 12 The variation of K^*_{II} under different **a** confining pressures and **b** axial compressive loads

$$K^{dp*}_{II}(t) = \alpha\sigma(t), \tag{4}$$

$$K^{dc*}_{II}(t) = \alpha\sigma(t) + \beta\sigma_c. \tag{5}$$

Thus, the loading rates in the dynamic PTS and SCC tests under the preload and the confinement can be determined by using these two equations, respectively. The slope of the linear region of the SIF-time curve is the loading rate. Figure 13 shows the loading rate determined in a typical dynamic PTS test with the preload. Also, the total fracture toughness of rocks under the preload (K_{IIC}^{tp}), the dynamic fracture toughness of rocks under the preload (K^{dp}_{IIC}), and the dynamic fracture toughness of rocks under the confinement (K_{IIC}^{dc}) can be derived from:
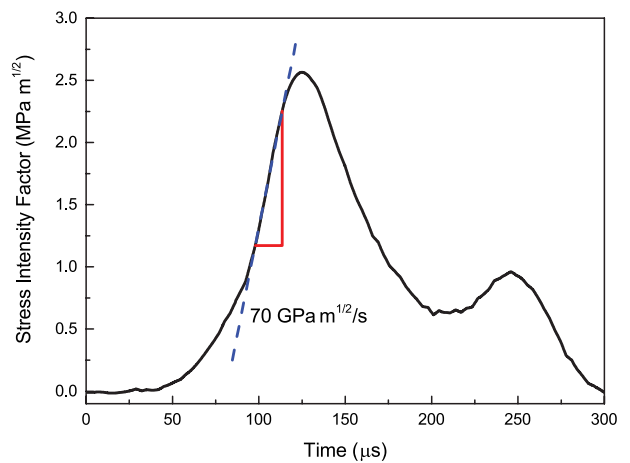

Fig. 13 Loading rate for a typical dynamic PTS test with the preload

$$K_{IIC}^{tp*} = \alpha\left(\sigma_{\max} + \sigma_{pre}\right), K_{IIC}^{dp*} = \alpha\sigma_{\max}, \tag{6}$$

$$K_{IIC}^{dc*} = \alpha\sigma_{\max} + \beta\sigma_c, \tag{7}$$

where $\sigma_{\max}$ is the peak dynamic compressive stress on the ends of PTS/SCC specimens (MPa), the values of α and β are the same as those in Eqs. (2) and (3).

4 Results and discussion

4.1 Dynamic mode II fracture toughness

With the momentum-trap system, the PTS and SCC specimens were soft-recovered after the dynamic tests with the preload. The tested PTS and SCC specimens are illustrated in Figs. 1c and 2b, respectively. After the dynamic mode II fracture tests with the preload, the PTS specimen was fractured in a short bar and a hollow cylinder, and the SCC specimen was broken along the potential fracture plane between these two notch-tips. The failure patterns of the PTS and SCC specimens are consistent with the corresponding failure modes reported in the existing studies (Xu et al. 2020; Yao et al. 2021, 2020, 2017). Based on the experimental observation in this study, the failure modes of the PTS and SCC specimens under both the dynamic loading and the preload are mode II. Further, in combination with the previous studies (Xu et al. 2020; Yao et al. 2021, 2020, 2017), it is proven that obviously valid are the dynamic mode II fracture toughnesses of rocks measured from both the dynamic PTS and SCC specimens under the preload and the confinement.

In the dynamic mode II experiments with preloads, the preloads for the PTS specimen are 0%, 20%, 40%, 60% and 80% P_{PTS}, and the preloads for the SCC specimen are 0%, 20%, 40%, 60% and 80% P_{SCC}. The dynamic fracture toughnesses K_{IIC}^{dp} of FM under various preloads measured in the

PTS and SCC experiments are shown in Fig. 14. In addition, the total fracture toughness K_{IIC}^{tp} of FM under different preloads represents the total loading capacity under superposed loading conditions, and the K_{IIC}^{tp} values of FM under various preloads measured in the PTS and SCC experiments are illustrated in Fig. 15. Meanwhile, the K_{IIC}^{dp} and K_{IIC}^{tp} of FM under various preloads obtained from the numerical models are shown in Figs. 14 and 15, respectively. Based on both the experimental and numerical results, under the same loading condition (including the dynamic loading rate and the preload level), the K_{IIC}^{dp} and K_{IIC}^{tp} of FM obtained from the numerical SCC model have a good agreement with the corresponding experimental results, indicating that the dynamic 2D numerical SCC model developed in this study is applicable and valid to obtain the dynamic mode II fracture toughness of rocks under various loading rates and preloads/confinements. Moreover, the K_{IIC}^{dp} and K_{IIC}^{tp} of FM measured from both PTS and SCC specimens with the preload increase with the loading rates, revealing that the K_{IIC}^{dp} and K_{IIC}^{tp} of FM has a strong rate dependence. The K_{IIC}^{dp} from the PTS specimen tends to increase linearly, whereas the K_{IIC}^{dp} from the SCC specimen is likely to increase logarithmically. One can see that under lower loading rates the K_{IIC}^{dp} and K_{IIC}^{tp} of FM measured from the PTS specimen are consistent with those measured from the SCC specimen under the same loading rate, whereas under higher loading rates, the K_{IIC}^{dp} and K_{IIC}^{tp} of FM measured from the PTS specimen are higher than those measured from the SCC specimen under the same loading rate. This phenomenon may be explained by the different sensitivity of K^*_{II} between the PTS and SCC specimens. As we discussed above, under the same axial compressive load, the K^*_{II} value in the PTS specimen is lower than that in the SCC specimen (Fig. 12b). The loading period at higher loading rates is shorter than that at lower loading rates and more microcracks are thus generated and activated under higher loading rates. Consequently, the sensitivity of K^*_{II} at the notch-tip plays an
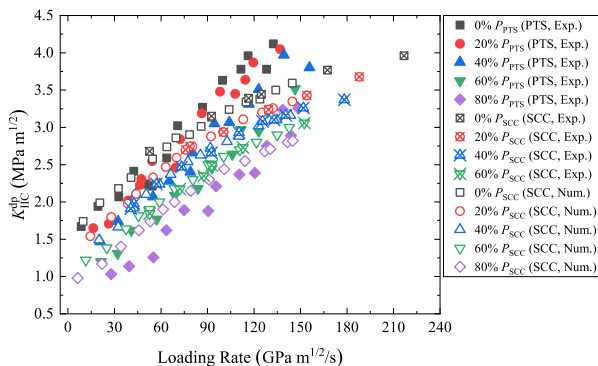

Fig. 14 Dynamic fracture toughness of FM obtained from PTS and SCC specimens with various preloads
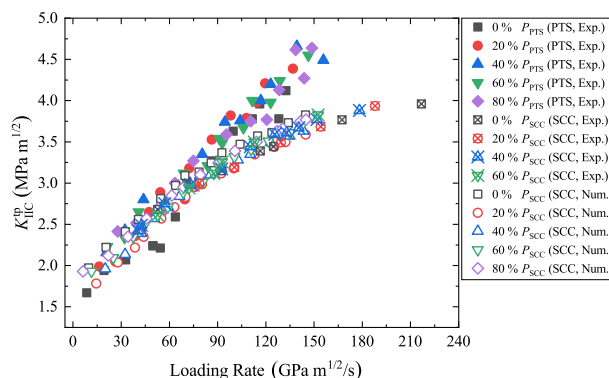

Fig. 15 Total fracture toughness of FM obtained from PTS and SCC specimens with various preloads

important role on the determination of the maximum axial compressive load when the PTS and SCC specimens fail under higher loading rates. The critical value of $K*_{\mathrm{II}}$ at the notch-tip in the SCC specimen is more easily reached than that in the PTS specimen. Therefore, the $K_{\mathrm{IIC}}^{\mathrm{dp}}$ and $K_{\mathrm{IIC}}^{\mathrm{tp}}$ of FM from the SCC specimen at higher loading rates are lower than those from the PTS specimen. Another important finding is that the $K_{\mathrm{IIC}}^{\mathrm{tp}}$ values of FM derived from the PTS/SCC specimen are almost consistent under the same loading rate regardless of the magnitude of the preload exerted on the PTS/SCC specimen. This phenomenon was also found in the dynamic tensile strength of granites under the static pretension using Brazilian disk (BD) specimens (Wu et al. 2015). This may be attributed to more microcracks produced and activated under preloads. With the increase of activated microcracks, the viscosity of the material is more sensitive to the loading rate, and thus the weakening effect due to the preload is compensated by the rate sensitivity induced by the material viscosity. Hence, the $K_{\mathrm{IIC}}^{\mathrm{tp}}$ values of FM under the same loading rate are roughly independent on the preload level (Wu et al. 2015).

The confining pressures applied on the PTS and SCC specimens were 0 MPa, 5 MPa, 10 MPa, 15 MPa, and 20 MPa, respectively. Figure 16 shows the dynamic mode II fracture toughness $K_{\mathrm{IIC}}^{\mathrm{dc}}$ of FM under various confining pressures. The $K_{\mathrm{IIC}}^{\mathrm{dc}}$ values of FM under confinements measured from the PTS specimen were reported in our previous study (Yao et al. 2020), while the $K_{\mathrm{IIC}}^{\mathrm{dc}}$ values of FM from the SCC specimen under the confinement are obtained by using the numerical simulation. For each confining pressure, the $K_{\mathrm{IIC}}^{\mathrm{dc}}$ of FM derived from the PTS and SCC specimens demonstrates a strong rate dependence, while the growth rate of the $K_{\mathrm{IIC}}^{\mathrm{dc}}$ from the PTS specimen in terms of the loading rate is significantly different from that from the SCC specimen. Furthermore, without the confining pressure, the $K_{\mathrm{IIC}}^{\mathrm{dc}}$ of FM from the PTS specimen are similar to that from the SCC specimen. However, the difference of the $K_{\mathrm{IIC}}^{\mathrm{dc}}$ between these two specimens becomes

larger and larger. The maximum $K_{\mathrm{IIC}}^{\mathrm{dc}}$ values are 8.59 MPa m$^{1/2}$ measured from the PTS specimen and 6.38 MPa m$^{1/2}$ obtained from the SCC specimen when the confining pressure is 20 MPa. The difference between these two maximum values is 2.21 MPa m$^{1/2}$. Hence, it is noteworthy that under the same loading rate and confinement (except for 0 MPa), the $K_{\mathrm{IIC}}^{\mathrm{dc}}$ of FM measured from the PTS specimen is generally greater than that from the SCC specimen, indicating that the $K_{\mathrm{IIC}}^{\mathrm{dc}}$ of FM using the PTS specimen is more sensitive to the confining pressure than that from the SCC specimen. This discrepancy may be attributed to the difference geometries of the PTS and SCC specimens. As illustrated in Fig. 12a, the sensitivity of the SIF at the notch-tip of the PTS specimen differs from that of the SCC specimen due to the distinct geometries, and the difference of the SIF at the notch-tip between these two specimens varies with the increase of the confining pressure. Thus, the difference of the $K_{\mathrm{IIC}}^{\mathrm{dc}}$ of FM between the PTS and SCC specimens under the same loading rate and confining pressure condition varies as the increase of the confining pressure, i.e., this difference is small when the PTS and SCC specimens are without confinement, and this difference is increasingly great with the increase of the confining pressure.

4.2 Reconciliation of Discrepancy of $K_{\mathrm{IIC}}^{\mathrm{dc}}$ Derived from PTS and SCC Methods

Another important contribution to the discrepancy of the $K_{\mathrm{IIC}}^{\mathrm{dc}}$ derived from PTS and SCC methods under the same loading rate and confinement may be the difference of the normal stress distribution induced by the confining pressure on the shear bridge of the PTS and SCC specimens. The normal stress distribution on the fracture surface of the PTS and SCC specimens under the same confining pressure $P_{\mathrm{c}} = 1$ MPa was analyzed and compared in Fig. 17. The cross-section of the shear bridge of the PTS specimen is a circle (Path 1 in Fig. 17a) and the cross-section of the shear bridge of the SCC specimen is a line (Path 2 in Fig. 17b). The normal stress applied on the shear bridge can be obtained directly from the confining pressure. Figure 17a shows that the normal stress on the shear fracture surface of the PTS specimen is uniform and equals to 1 MPa, whereas the normal stress on the shear fracture surface of the SCC specimen is not uniform as shown in Fig. 17b. The maximum normal stress on the shear fracture surface of the SCC specimens is 1 MPa at the center of the specimen and the normal stress decreases progressively to the left and right of the shear fracture surface. Obviously, the average normal stress caused by the confinement on Path 1 is 1 MPa. On the contrary, the average normal stress caused by the confinement on Path 2 is 0.64 MPa even if the confinement is 1 MPa. Consequently, the normal stress on the shear fracture of the PTS specimen is significantly different from that of
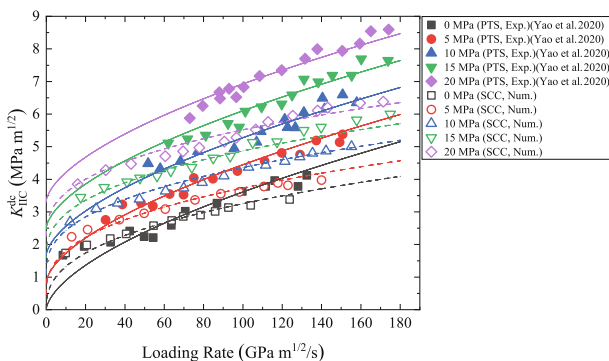

Fig. 16 Dynamic fracture toughness obtained from PTS and SCC specimens with various confining pressures
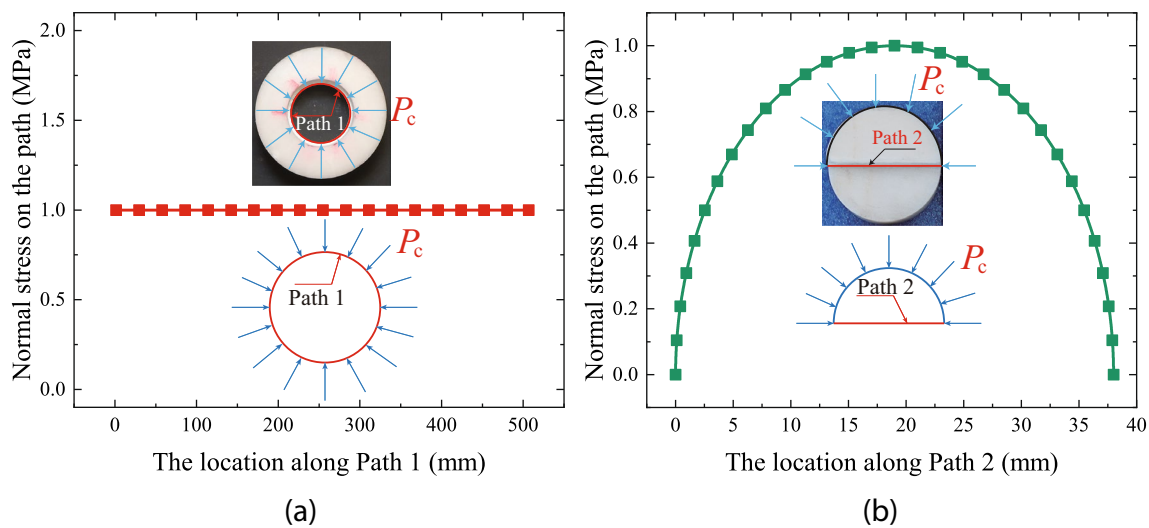
Fig. 17 Distribution of normal stress on the shear bridge of **a** PTS specimen and **b** SCC specimen due to the confining pressure

the SCC specimen even if the confining pressure exerted on these two specimens is the same, which is determined by the geometry of the specimen. As a result, the K_{IIC}^{dc} obtained from the PTS under the same loading rate and confinement is quite distinct from that from the SCC specimen, and this discrepancy becomes increasingly apparent with the increase of the confinement pressure.

It has been proven that both the PTS and SCC methods are valid to measure the dynamic fracture toughness of rocks without the confinement and the values of the dynamic fracture toughness of rocks derived from these two methods without the confinement are almost consistent. These two specimens are validly applied to assess the dynamic fracture toughness of rocks under various confinement conditions, which are widely encountered in underground rock engineering practices. Meanwhile, the discrepancy of the dynamic fracture toughness of rocks under the confinement between the PTS and SCC methods is mainly caused by the different geometries and normal stresses between these two specimens. In such case, it is necessary to reconcile the difference of the dynamic fracture toughness of rocks under the confinement measured from these two methods. A formula is established to predict the K_{IIC}^{dc} of rocks under various confinements and loading rates for both the PTS and SCC specimens:

$$
\begin{aligned}
K_{IIC}^{dc} &= \left[\eta G^a + \lambda R^b + \gamma Q^c \right] \times K_{IIC}^s \\
&= \left[\eta \left(\frac{C}{H} \right)^a + \lambda \left(\frac{\dot{K}_{II}}{\dot{K}_C} \right)^b + \gamma \left(\frac{\sigma_c}{P_0} \right)^c \right] \times K_{IIC}^s,
\end{aligned}
\tag{8}
$$

where $G = C/H$ characterizes the PTS or SCC specimen geometry, C is the length of the shear fracture bridge (i.e., $C = 10$ mm for the PTS specimen and $C = 7.6$ mm for the SCC

specimen), H is the length of the specimen (i.e., $H = 30$ mm for the PTS specimen and $H = 38$ mm for the SCC specimen), $C/H = 0.33$ for the PTS specimen, $C/H = 0.2$ for the SCC specimen; R represents the loading rate effect, $\dot{K}_{II}$ is the loading rate, $\dot{K}_C = 0.01$ GPa m$^{1/2}$/s is the reference loading rate; Q is the confinement effect, σ_c is the confining pressure and $P_0 = 1$ MPa is the reference pressure; KS IIC is the static mode II fracture toughness of rocks measured from the PTS or SCC specimens; a, b, c, η, λ and γ are fitting parameters, which are determined by using Genetic algorithm. For the PTS specimen, one group of valid values of these fitting parameters is $\eta = 2.4716$, $a = -0.3028$, $\lambda = 2.8678$, $b = 0.4167$, $\gamma = -0.5710$, $c = 0.7762$; for the SCC specimen, one group of valid values of these fitting parameters is $\eta = 2.1744$, $a = -0.6103$, $\lambda = 0.1992$, $b = 0.7136$, $\gamma = 0.0811$, $c = 0.8493$. This formula comprehensively reflects the geometrical effect (the first term), the loading rate effect (the second term) and the confinement effect (the third term). One group of the suitable values for the fitting parameters indicate that this formula can be valid to predict the data points as the fitting curves shown in Fig. 16. It is clear that the curves provide good predictions for the date point for both the PTS and SCC specimens. Furthermore, based on Eq. (8) with the fitting parameters and the values of the KS IIC measured from the PTS and SCC specimens, the K_{IIC}^{dc} from the PTS specimen under a certain loading rate and a given confinement can be predicted by using the K_{IIC}^{dc} value measured from the SCC specimen at the corresponding condition, and vice versa. In other words, if the KS IIC values measured from the PTS and SCC specimens are known and the K_{IIC}^{dc} value measured from the SCC specimen under a certain loading rate and a given confinement is also known, the K_{IIC}^{dc} from the PTS specimen at the corresponding loading condition

can be predicted by using Eq. (8), and vice versa. When the geometrical parameter G and the fitting parameters are known for both the PTS and SCC specimens, the $K_{\mathrm{IIC}}^{\mathrm{dc}}$ value for both these two methods under various loading rates and confining pressures can be determined by using the ratio of the KS IIC from the PTS specimen to the KS IIC from the SCC specimen. Namely, if the KS IIC value, the geometrical parameter G and the fitting parameters are known for both the PTS and SCC specimens, the $K_{\mathrm{IIC}}^{\mathrm{dc}}$ values for the PTS (or SCC) specimen under various loading rates and confining pressures can be determined by using the $K_{\mathrm{IIC}}^{\mathrm{dc}}$ values for the SCC (or PTS) specimen under the corresponding loading rates and confining pressures. Therefore, according to Eq. (8) and the values of KS IIC from both the PTS and SCC specimens, the relationship between the $K_{\mathrm{IIC}}^{\mathrm{dc}}$ value from the PTS specimen and the corresponding $K_{\mathrm{IIC}}^{\mathrm{dc}}$ value from the SCC specimen can be established if the rock specimen is under the same loading rate and confining pressure. Also, the $K_{\mathrm{IIC}}^{\mathrm{dc}}$ value from the SCC specimen can be converted into the corresponding value obtained by the PTS method at the same loading and confinement condition.

5 Conclusions

In this study, two dynamic mode II fracture methods (i.e., the punch-through shear (PTS) method and the short core in compression (SCC) method) were applied to obtain the dynamic mode II fracture toughness of Fangshan Marble (FM) under the preload or the confinement. The dynamic mode II fracture tests were performed by using the dynamic-static-combined test apparatus. Different preload values were determined based on the static critical load of the PTS/SCC specimen. Due to the limitation of the existing triaxial SHPB apparatus and the geometry of the SCC specimen, the numerical simulation was used to mimic the dynamic SCC-SHPB tests with high confinements.

The shear stress fields of the PTS and SCC specimens under different confining pressures were systematically compared. With the increase of the preload/the confining pressure, the shear stress increases for both the PTS and SCC specimens. The stress intensity factors generated at the notch-tips are distinct in these two types of specimens under the same loading force and confining pressure. This causes that the critical load of the PTS specimen differs from that of the SCC specimen. Also, it is noteworthy that the shear stresses generated at the notch-tips are distinct in these two types of specimens at the same percentage of the corresponding critical load.

Under the same dynamic loading rate and preload, the dynamic fracture toughness $K^{\mathrm{dp}}_{\mathrm{IIC}}$ and the total fracture toughness $K_{\mathrm{IIC}}^{\mathrm{tp}}$ of FM derived from the SCC numerical model have a good agreement with the corresponding experimental results, indicating that the dynamic 2D numerical SCC model developed in this study is applicable and valid to obtain the dynamic mode II fracture toughness of rocks under various loading rates and preloads/confinements. The $K^{\mathrm{dp}}_{\mathrm{IIC}}$ and $K_{\mathrm{IIC}}^{\mathrm{tp}}$ of FM measured from both PTS and SCC specimens with the preload increase with the loading rates. Under lower loading rates, the $K^{\mathrm{dp}}_{\mathrm{IIC}}$ and $K_{\mathrm{IIC}}^{\mathrm{tp}}$ of FM measured from the PTS specimen are consistent with those measured from the SCC specimen, whereas under higher loading rates, the $K^{\mathrm{dp}}_{\mathrm{IIC}}$ and $K^{\mathrm{tp}}_{\mathrm{IIC}}$ of FM measured from the PTS specimen are higher than those measured from the SCC specimen. This phenomenon may be explained by the different sensitivity of the stress intensity factor between the PTS and SCC specimens. Another important finding is that the $K_{\mathrm{IIC}}^{\mathrm{tp}}$ values of FM derived from the PTS/SCC specimen are almost consistent under the same loading rate regardless of the magnitude of the preload exerted on the PTS/SCC specimen.

For each confining pressure, the dynamic fracture toughness $K_{\mathrm{IIC}}^{\mathrm{dc}}$ of FM derived from both the PTS and SCC specimens demonstrates a strong rate dependence, while the growth rate of the $K_{\mathrm{IIC}}^{\mathrm{dc}}$ of FM from the PTS specimen under the same loading rate and confinement is significantly different from that from the SCC specimen. This discrepancy may be attributed to the difference geometries of the PTS and SCC specimens and the difference of the stress distribution induced by the confining pressure on the shear bridge of the PTS and SCC specimens. Furthermore, a formula is established to predict the $K_{\mathrm{IIC}}^{\mathrm{dc}}$ of rocks under various confinements and loading rates for both the PTS and SCC specimens. This formula comprehensively reflects the geometrical effect, the loading rate effect and the confinement effect. The relationship between the $K_{\mathrm{IIC}}^{\mathrm{dc}}$ of rocks measured from the PTS specimen and the SCC specimen can be established when the rock specimen is under the same loading rate and confining pressure.

Declarations

References

Anderson T (2005) Fracture mechanics. Fundamentals and applications. CRC Press

Azar HF, Choupani N, Afshin H, Moghadam RH (2015) Effect of mineral admixtures on the mixed-mode (I/II) fracture characterization of cement mortar: CTS, CSTBD and SCB specimens. Eng Fract Mech 134:20–34

Backers T (2005) Fracture toughness determination and micromechanics of rock under mode I and mode II loading. Universty of Postdam

Backers T, Stephansson O (2012) ISRM suggested method for the determination of mode II fracture toughness. Rock Mech Rock Eng 45:1011–1022

Backers T, Stephansson O, Rybacki E (2002) Rock fracture toughness testing in mode II—punch-through shear test. Int J Rock Mech Min Sci 39:755–769

Backers T, Dresen G, Rybacki E, Stephansson O (2004) New data on mode II fracture toughness of rock from the punchthrough shear test. Int J Rock Mech Min Sci 41:2–7. https://doi.org/10.1016/j.ijrmms.2004.03.010

Chang S-H, Lee C-I, Jeon S (2002) Measurement of rock fracture toughness under modes I and II and mixed-mode conditions by using disc-type specimens. Eng Geol 66:79–97

Chen F, Cao P, Rao QH, Ma CD, Sun ZQ (2004) A mode II fracture analysis of double edge cracked Brazilian disk using the weight function method. Int J Rock Mech Min Sci 42:461–465

Chen R, Li K, Xia K, Lin Y, Yao W, Lu F (2016) Dynamic fracture properties of rocks subjected to static pre-load using notched semi-circular bend method. Rock Mech Rock Eng 49:3865–3872

Davies J, Morgan TG, Yim AW (1985) The finite element analysis of a punch-through shear specimen in mode II. Int J Fract 28:R3–R10

Deng CJ, He GJ, Zheng YR (2006) Study on the Drucker-prager yield criterions based on the M-C yield. Chin J Geotech Eng 06:735–739

Fakhri M, Amoosoltani E, Aliha MRM (2017) Crack behavior analysis of roller compacted concrete mixtures containing reclaimed asphalt pavement and crumb rubber. Eng Fract Mech 180:43–59

Fowell RJ (1995) Suggested method for determining mode I fracture toughness using Cracked Chevron Notched Brazilian Disc (CCNBD) specimens. Int J Rock Mech Min Sci Geomech Abstracts 32:57–64

Franklin JA, Sun Z, Atkinson BK, Meredith PG, Bobrov GF (1988) Suggested methods for determining the fracture toughness of rock. Int J Rock Mech Min Sci Geomech Abstracts 25:71–96

Frew DJ, Akers SA, Chen W, Green ML (2010) Development of a dynamic triaxial Kolsky bar. Meas Sci Technol 21:105704. https://doi.org/10.1088/0957-0233/21/10/105704

Hasanpour R, Choupani N (2008) Rock fracture characterization using the modified Arcan test specimen. Int J Rock Mech Min Sci 46:346–354

Heritage Y (2019) Mechanics of rib deformation—observations and monitoring in Australian coal mines. Int J Min Sci Technol 29:119–129. https://doi.org/10.1016/j.ijmst.2018.11.017

Jung Y, Park E, Kim H (2016) Determination of mode II toughness of granite by using SCC test. In: Proceedings of the ISRM International Symposium - EUROCK 2016, Ürgüp, p 271

Kim B-H, Larson M (2021) Laboratory investigation of the anisotropic confinement-dependent brittle-ductile transition of a Utah coal. Int J Min Sci Technol 31:51–57. https://doi.org/10.1016/j.ijmst.2020.12.017

Kuruppu MD, Obara Y, Ayatollahi MR, Chong KP, Funatsu T (2014) ISRM-suggested method for determining the mode I static fracture toughness using semi-circular bend specimen. Rock Mech Rock Eng 47:267–274

Lee JS (2007) Time-dependent crack growth in brittle rocks and field applications to geologic hazards. The University of Arizona

Li X, Zhou Z, Lok T-S, Hong L, Yin T (2007) Innovative testing technique of rock subjected to coupled static and dynamic loads. Int J Rock Mech Min Sci 45:739–748

Li D, Gao F, Han Z, Zhu Q (2020a) Experimental evaluation on rock failure mechanism with combined flaws in a connected geometry under coupled static-dynamic loads. Soil Dyn Earthq Eng 132:106088. https://doi.org/10.1016/j.soildyn.2020.106088

Li D, Gao F, Han Z, Zhu Q, Karinski YS (2020b) Full- and local-field strain evolution and fracture behavior of precracked granite under coupled static and dynamic loads. Shock Vib 2020:1–15. https://doi.org/10.1155/2020/8866673

Lukić B, Forquin P (2016) Experimental characterization of the punch through shear strength of an ultra-high performance concrete. Int J Impact Eng 91:1–10

Mostafavi M, McDonald SA, Mummery PM, Marrow TJ (2013) Observation and quantification of three-dimensional crack propagation in poly-granular graphite. Eng Fract Mech 110:410–420

Peng X, Yuan LD, Yan ZG, Qi ZQ, Xin LH, Shun ZC (2020) Mechanical properties and failure behavior of rock with different flaw inclinations under coupled static and dynamic loads. J Central South Univ 27:2945–2958

Pirmohammad S, Abdi M, Ayatollahi MR (2021) Mode II fracture tests on asphalt concrete at different temperatures using semi-circular bend specimen loaded by various types of supports. Theoret Appl Fract Mech 116:103089. https://doi.org/10.1016/j.tafmec.2021.103089

Rao Q, Sun Z, Stephansson O, Li C, Stillborg B (2003) Shear fracture (Mode II) of brittle rock. Int J Rock Mech Min Sci 40:1–8

Razavi SMJ, Aliha MRM, Berto F (2017) Application of an average strain energy density criterion to obtain the mixed mode fracture load of granite rock tested with the cracked asymmetric four-point bend specimens. Theoret Appl Fract Mech 97:419–425

Shi YW, Zhou NN (1995) Comparison of microshear toughness and mode II fracture toughness for structural steels. Eng Fract Mech 51:669–677

Su JH, Wang ZX, Ren WM (2003) Study and application of yield criteria to rock and soil. Chin J Eng Mech 20:72–77

Swartz SE, Lu LW, Tang LD, Refai TME (1988) Mode II fracture-parameter estimates for concrete from beam specimens. Exp Mech 28:146–153

Szwedzicki T (2003) Quality assurance in mine ground control management. Int J Rock Mech Min Sci 40:565–572. https://doi.org/10.1016/S1365-1609(03)00026-1

Watkins J, Liu KLW (1985) A finite element study of the short beam test specimen under mode II loading. Int J Cem Compos Lightweight Concrete 7:1–6

Wei M-D, Dai F, Xu N-W, Zhao T (2016a) Stress intensity factors and fracture process zones of ISRM-suggested chevron notched specimens for mode I fracture toughness testing of rocks. Eng Fract Mech 168:174–189

Wei MD, Dai F, Xu NW, Zhao T, Xia KW (2016b) Experimental and numerical study on the fracture process zone and fracture toughness determination for ISRM-suggested semi-circular bend rock specimen. Eng Fract Mech 154:43–56

Wei M-D, Dai F, Xu N-W, Liu Y, Zhao T (2017) Fracture prediction of rocks under mode I and mode II loading using the generalized maximum tangential strain criterion. Eng Fract Mech 186:21–38

Whittaker BN, Singh RN, Sun G (1992) Rock fracture mechanics. Principles, design and applications. Elsevier Science Publishers, Amsterdam

Wu B, Chen R, Xia K (2015) Dynamic tensile failure of rocks under static pre-tension. Int J Rock Mech Min Sci 80:12–18. https://doi.org/10.1016/j.ijrmms.2015.09.003

Xie Y, Cao P, Jin J, Wang M (2017) Mixed mode fracture analysis of semi-circular bend (SCB) specimen: a numerical study based on extended finite element method. Comput Geotech 82:79–96

Xu NW, Dai F, Wei MD, Xu Y, Zhao T (2016) Numerical observation of three-dimensional wing cracking of cracked chevron notched Brazilian disc rock specimen subjected to mixed mode loading. Rock Mech Rock Eng 49:79–96

Xu Y, Yao W, Zhao G, Xia K (2020) Evaluation of the short core in compression (SCC) method for measuring mode II fracture toughness of rocks. Eng Fract Mech 224:258–364. https://doi.org/10.1016/j.engfracmech.2019.106747

Yao W, Xu Y, Yu C, Xia K (2017) A dynamic punch-through shear method for determining dynamic mode II fracture toughness of rocks. Eng Fract Mech 176:161–177

Yao W, Xia K, Zhang T (2019) Dynamic fracture test of Laurentian granite subjected to hydrostatic pressure. Exp Mech 59:245–250. https://doi.org/10.1007/s11340-018-00437-4

Yao W, Xu Y, Xia K, Wang S (2020) Dynamic mode II fracture toughness of rocks subjected to confining pressure. Rock Mech Rock Eng 53:569–586. https://doi.org/10.1007/s00603-019-01929-y

Yao W, Xu Y, Wang C, Xia K, Hokka M (2021) Dynamic Mode II fracture behavior of rocks under hydrostatic pressure using the short core in compression (SCC) method. Int J Min Sci Technol 31:927–937. https://doi.org/10.1016/j.ijmst.2021.08.001

Yin T, Bai L, Li X, Li X, Zhang S (2018) Effect of thermal treatment on the mode I fracture toughness of granite under dynamic and static coupling load. Eng Fract Mech 199:143–158

Zhang QBZJ (2013a) Determination of mechanical properties and full-field strain measurements of rock material under dynamic loads. Int J Rock Mech Min Sci 60:423–439

Zhang QBZJ (2013b) Effect of loading rate on fracture toughness and failure micromechanisms in marble. Eng Fract Mech 102:288–309

Zhang ZX, Kou SQ, Yu J, Yu Y, Jiang LG, Lindqvist P-A (1999) Effects of loading rate on rock fracture. Int J Rock Mech Min Sci 37:745–762

Zhou YX, Xia K, Li XB, Li HB, Ma GW, Zhao J, Zhou ZL, Dai F (2012) Suggested methods for determining the dynamic strength parameters and mode-I fracture toughness of rock materials. Int J Rock Mech Min Sci 49:105–112. https://doi.org/10.1016/j.ijrmms.2011.10.004

Zhou Z, Li X, Zou Y, Jiang Y, Li G (2014) Dynamic Brazilian tests of granite under coupled static and dynamic loads. Rock Mech Rock Eng 47:495–505

Zhou Z, Cai X, Li X, Cao W, Du X (2020) Dynamic response and energy evolution of sandstone under coupled static-dynamic compression: insights from experimental study into deep rock engineering applications. Rock Mech Rock Eng 53:1305–1331. https://doi.org/10.1007/s00603-019-01980-9